Li, Feitao; Oliva Ramírez, Manuel; Wang, Dong; Schaaf, Peter

Formation and evolution of Au-SiOx heterostructures: from nanoflowers to nanosprouts

Original published in:	Materials and design. - Amsterdam [u.a.] : Elsevier Science. - 209 (2021), art. 109956, 11 pp.
Original published:	2021-07-03
ISSN:	1873-4197
DOI:	10.1016/j.matdes.2021.109956
[*Visited:*	2022-03-08]

Materials & Design 209 (2021) 109956

Contents lists available at ScienceDirect

Materials & Design

journal homepage: www.elsevier.com/locate/matdes

Formation and evolution of Au-SiO_x Heterostructures: From nanoflowers to nanosprouts

Feitao Li, Manuel Oliva-Ramírez *, Dong Wang *, Peter Schaaf

Chair Materials for Electrical Engineering and Electronics, Institute of Materials Science and Engineering and Institute of Micro- and Nanotechnologies MacroNano®, TU Ilmenau, Gustav-Kirchhoff-Strasse 5, 98693 Ilmenau, Germany

HIGHLIGHTS

- Novel sprout-like structure was produced by rapid annealing in a reducing atmosphere.
- Two Si sources contribute to the formation of SiO_x nanowires.
- Volatile SiO moves to the surface by defect-mediated diffusing along the SiO_2 layer.
- Direction change of the main Si source relative to structures splits the particles.

GRAPHICAL ABSTRACT

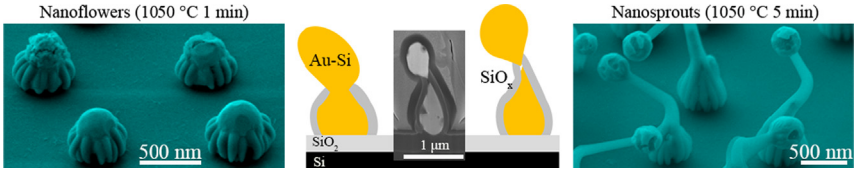

ARTICLE INFO

Article history:
Received 22 April 2021
Revised 22 June 2021
Accepted 2 July 2021
Available online 3 July 2021

Keywords:
SiO_2 decomposition
Vapor–liquid–solid
Si active oxidation
Au silicide
Dewetting

ABSTRACT

This work reports the formation of circular cavities and Au-SiO_x nanoflowers after annealing of thin Au film deposited on SiO_2/Si substrates, and the transformation of nanoflowers to nanosprouts with increasing the annealing time. Two reference experiments indicate that both H_2 and Si are indispensable for the above structures. The formation of cavities can be attributed to the SiO_2 layer decomposition and the product, volatile SiO, provides a Si source for the formation of nanoflowers at the early stage. A model is proposed to indicate that SiO gas produced at the Si/SiO_2 interface can diffuse to the surface assisted by the defects in the SiO_2 layer before the decomposed cavities are exposed. Then the exposing of those cavities introduces another volatile SiO from the active oxidation of Si substrate, provoking a change in the direction of the main Si source, which in turn makes the one nanoparticle of the nanoflower split in two and finally form the nanosprout. The model about the escape of SiO further details SiO_2 decomposition process, and the transformation mechanism from nanoflowers to nanosprout sheds light on a feasible nanofabrication method to design tunable size and shape of nanoparticles.

1. Introduction

Nanowires (NWs) have been profoundly investigated within the past two decades due to their extremely attractive application prospects in different kinds of nanoscale devices [1–5]. Among them, Silicon (Si) and Si oxide (SiO_x) NWs are typical hotspots of research due to their potentiality as crucial components in nanoelectronic devices [6–9]. These NWs mainly form by two mechanisms, the vapor–liquid–solid (VLS) [10,11] and the oxide-assisted growth (OAG) [12]. The VLS mechanism describes a process at a temperature slightly above the Au-Si eutectic point in which the Si goes through three stages. First, Si is introduced from a gas source, then it is absorbed by a catalyst (such as Au nanoparticles) forming a eutectic droplet, and finally, it precipitates as solid Si or SiO_x NWs. Although minor discrepancies still exist for the VLS mechanism when it comes to different synthesis situations, the above mentioned three stages are widely accepted by the academic community. Based on the VLS mechanism, several kinds of nanostruc-

* Corresponding authors.
E-mail addresses: manuel.oliva-ramirez@tu-ilmenau.de (M. Oliva-Ramírez), dong.wang@tu-ilmenau.de (D. Wang).

https://doi.org/10.1016/j.matdes.2021.109956
0264-1275/

tures, like octopus-like [13], lantern-like [14] and flower-like [15], had been successfully synthesized. Another route to grow NWs is based on the OAG mechanism, which consists of the thermal sublimation of silicon monoxide (SiO) powder or laser ablation of Si and SiO_2 powders, synthetizing Si-SiO_2 core–shell NWs without needing a catalyst [16,17]. Therefore, the distinct morphologies of the nanostructures grown by both mechanisms prove that Si source plays a crucial role in the synthesis of Si or SiO_x NWs and also for their morphologies.

In addition, both interaction between Si and deposited materials [18], and thermal stability between Si and a Si dioxide (SiO_2) layer [19–22] play important roles for the fabrication process and the reliability of the nanoscale devices. SiO_2 layers could react with Si substrates at high temperatures and high vacuum or low oxygen partial pressures, which leads to the formation of multiple cavities in the SiO_2 layer [19]. These cavities result from the decomposition reaction $Si + SiO_2 \rightarrow 2SiO_{(g)}$ and are initiated at pre-existing defects of the SiO_2/Si interface, presenting a heterogeneous distribution all over the substrate [23,24]. Once the cavities are formed, the decomposition proceed at their periphery according to the diffusion of Si from their centers to the borders, resulting in the radial expansion of the cavities. Some metallic thin films deposited on top of the SiO_2 layer may accelerate its decomposition rate due to the diffusion of metal atoms to the SiO_2/Si interface assisted by occurring microchannels and microvoids in the oxide layer [25–27]. The volatile SiO produced in that reaction may act as a potential Si source for the formation of NWs in an analogous way to the Si sources of the OAG mechanism [16,17]. However, the decomposition of the native SiO_2 layer (about 3 nm) on Si surface was believed to be only a negligible Si source [28], while in another work with much thicker SiO_2 layers, authors only focused on the dynamics of the Au droplet formation and did not report any information about NWs [29]. There is no known research combining two or more Si sources for the synthesis of NWs either. Some works combined SiO with Au catalyst to fabricate nanostructures, but the volatile SiO in those studies came from the active oxidation of the Si substrate ($2Si + O_2 \rightarrow 2SiO_{(g)}$) [15,28]. Therefore, it should be interesting to design Au/SiO_2/Si systems with a thick SiO_2 layer. There, Si sources from both processes, decomposition and active oxidation, may act together and alternate their roles as the main Si source, with subsequent effects on the morphology of the forming structures.

In the present work, two kinds of Au-SiO_x nanostructures made of nanoparticles and NWs are synthesized from a thin Au film deposited onto the SiO_2(200 nm)/Si substrate by annealing at 1050 °C in a reducing environment. After annealing for short times, flower-like nanostructures consisting of a central nanoparticle and surrounding SiO_x NWs are synthesized. Increasing annealing times leads to the growth of a nanowire from the flower-like nanostructure with a nanoparticle on top presenting the shape of a sprout-like nanostructure. The evolution between these two nanostructures is attributed to the change in the direction of the incoming Si source which is closely related to the decomposition of the SiO_2 layer. Volatile SiO initially comes from the decomposition and is transported through the defects in the SiO_2 layer. After the piercing of decomposing cavities, the volatile SiO from the active oxidation of the Si also desorbs into the atmosphere, resulting in a change in the direction of the incoming Si source from the bottom to the top, which eventually splits the nanoparticle of the flower-like nanostructure in two. This new split nanoparticle is elevated by the merging of the surrounding SiO_x NWs, and thus forms the above-mentioned sprout-like nanostructure. These findings may provide a route for the fabrication of these nanostructures and also propose the unraveled role of the incoming Si sources as a tool for the design of nanostructures.

2. Materials and methods

20 nm Au thin film was deposited on single-side polished p-type Si substrate with (1 0 0) orientation by electron beam evaporation (CS400ES, VON ARDENNE) at a working pressure of $1{\cdot}10^{-6}$ mbar. A 200 nm SiO_2 layer was thermally grown before the thin film deposition. The morphology and EDS results as well as XRD spectrum of as-deposited sample are shown in Fig. 1(a-c). Both EDS and XRD results indicate that there is only Au phase existing in the as-deposited sample besides the SiO_2/Si substrate. The XRD result also shows that Au grains are highly textured along the (1 1 1) orientation in the as-deposited sample [30].

The as-deposited samples were annealed in a rapid thermal processing (RTP, Jipelec Jetstar 100) furnace. Firstly, the chamber was evacuated and purged by Argon (Ar, purity: 6 N) several times, then a flow of forming gas (Ar and hydrogen (H_2, purity: 5 N)) with a volume ratio of 30:1 was kept during the whole annealing period. The temperature was directly increased to 1050 ℃ from room temperature within 20 s and then held for different annealing times (30 s, 60 s, 120 s and 300 s). Finally, the heating was switched off and the temperature decreased at different rates for each sample. The cooling periods consist of initially fast cooling of about 15 K/s, followed by a slower cooling of about 1 K/s. The detailed heat treatment curves in Fig. 1(d) indicate that the fast cooling lasts longer for shorter annealing times because there is more residual heat inside the annealing chamber for longer annealing times [31]. Each system is labeled by its annealing time, e.g., the sample annealed for 30 s will be named 30 s sample. Further reference experiments were performed by using analogous layers deposited on fused silica (SiO_2) substrates and by annealing in oxygen (O_2, purity: 4.8 N) atmosphere to unravel the roles of the Si substrate and H_2 reducing atmosphere, respectively. The annealing parameters, 1050 ℃ and 60 s, were chosen for both reference experiments. The bare SiO_2(200 nm)/Si substrates were also treated in RTP by using the same annealing parameters with those samples covered by the Au thin film.

The morphology of the surfaces of the annealed samples was obtained by high-resolution scanning electron microscopy (SEM, Hitachi S-4800), equipped with energy-dispersive X-ray spectroscopy (EDS, Thermo Scientific). SEM images were taken at low acceleration voltage (1.5 kV) to avoid charging effects using both secondary electron (SE) and backscattered electron (BSE) detectors to register morphology and material contrast, respectively. The region consisting of elements with higher atomic numbers show brighter contrast. EDS scanning was performed at 7 kV to obtain the signals from the M_α line of Au and K_α lines of Si and oxygen (O). Cross-sectional cut was performed with a focused ion beam (FIB, Zeiss Auriga 60 dual beam) device to analyze the internal morphology of the particles. Before cutting, protective carbon and platinum layers were deposited sequentially. XRD diffractograms (Siemens D-5000) were recorded at Bragg-Brentano configuration mode using Cu K_α irradiation at 40 kV. A profilometer (Dektak 150) equipped with a 10 μm detector was used to get the height distribution across the decomposed cavities.

3. Results and discussion

Fig. 2 shows the top and tilted views of samples annealed at 1050 ℃ for four increasing annealing times that present nanoparticles and NWs of different morphologies. The 30 s sample in Fig. 2(a) exhibits a type of nanostructures consisting of a spherical nanoparticle surrounded by multiple wires. This makes the whole nanostructure looking like a flower-like morphology, referred to as nanoflower. The 60 s sample also presents these nanoflowers, and Fig. 2(b) shows their surrounding NWs become longer than those

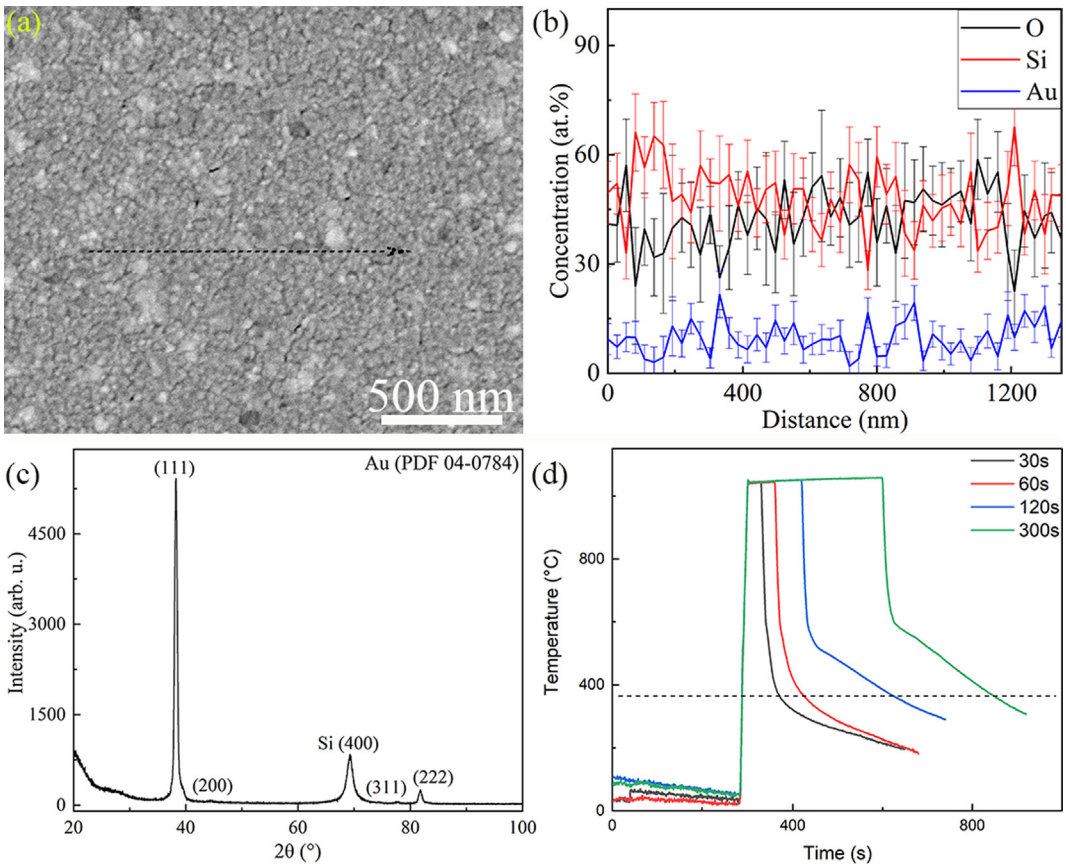

Fig. 1. SEM image (a), EDS (b) and XRD (c) results of as-deposited samples. (d) Heat treatment curves of the four samples in RTP. The dashed line in (d) is the Au-Si eutectic temperature.

grown in the 30 s sample. The tilted view of the nanoflowers formed in the 60 s sample in Fig. 2(e) shows how the NWs grow along the surface of the central nanoparticles and cover their lower part. Those surrounding NWs, they will be addressed as nanobranches, present a difference in size for the above two samples, as expected for a time dependent. Additionally, the difference of the surface morphology in the upper part of the nanoparticles is also clear in Fig. 2(e). The upper part of some particles presents a smooth surface while others show rough surfaces exhibiting cracks and inhomogeneities. More details about this surface difference will be discussed below. The longer annealing time of the 120 s sample leads to the growth of a different nanostructure besides the nanoflowers. The new nanostructure presents a nanoflower from where a nanowire grows with a nanoparticle on its top. The whole structure shows a sprout-like shape, and thus will be labeled as nanosprout. The 300 s system only presents this kind of nanosprouts and the tilted view of Fig. 2(f) clearly shows how the nanoflower acts as base of the nanosprouts. This tilted view presents several material contrasts in the top nanoparticle and the nanoflower base as well as in the middle nanowire, which indicates the presence of different phases distributed along the structures. These results suggest that the flower-like structure evolves to the sprout-like structure with increasing annealing time.

The XRD diffractograms of the systems in Fig. 3 show that the Au phase presents changes in intensity of the reflexes belonging to the (111) orientation that imply a change in texturing [30]. The intensity ratios of Au (111)/(200) of the systems in Table 1 shows that the Au phase is textured in the direction (111) in all the systems. However, as the annealing time increases, the ratios gradually decrease from nanoflowers (30 s and 60 s) to nanosprouts (300 s). This decrease can be attributed to the growth of the surrounding nanobranches which not only breaks the central nanoparticles (Fig. 2(e)), but also elevates the top particles (Fig. 2(f)), which in turn changes the initial orientation of the particles and weaken the texture. Besides, the reflexes around 27.7° (reflex 1) and 42.1° (reflex 2), which can be identified as Au silicide [32,33], practically disappear after 120 s. Therefore, based on XRD results, in 30 s and 60 s samples coexist two phases, Au and Au silicide. By contrast, only Au can be detected by XRD scanning in the 300 s sample.

Once the present phases are determined by XRD, their distribution in the nanoflowers will be determined by the EDS line scans and the cross-sectional views of Fig. 4. Fig. 4(a) shows two neighboring nanoflowers with distinct morphologies and Fig. 4(b) exhibits that the central nanoparticles of nanoflowers are rich in Au. Especially for the nanoparticle of the nanoflower with a smooth surface, the Au concentration is much higher than that of the rough one. The distributions of the other expected elements in the nanoflowers in Fig. 4(b) and Fig. S1 exhibits that there is higher oxygen concentration in the rough nanoflower than in the smooth counterpart, while the concentrations of Si in the two nanoflowers are close to each other. Fig. 4(c-d) show the cross-sectional views of nanoflowers outlined in boxes of Fig. 2(e), which indicate that nanoflowers with different surface morphologies present different phases in their inside according to the material contrasts. The smooth nanoflower presents a bright contrast on the top and a dark contrast on the bottom, while the rough nanoflower shows a dark contrast on the top and bright contrast on the bottom. Moreover, the dark areas of the rough nanoflower in Fig. 4(d) are separated into many small pieces by the bright area. Considering the

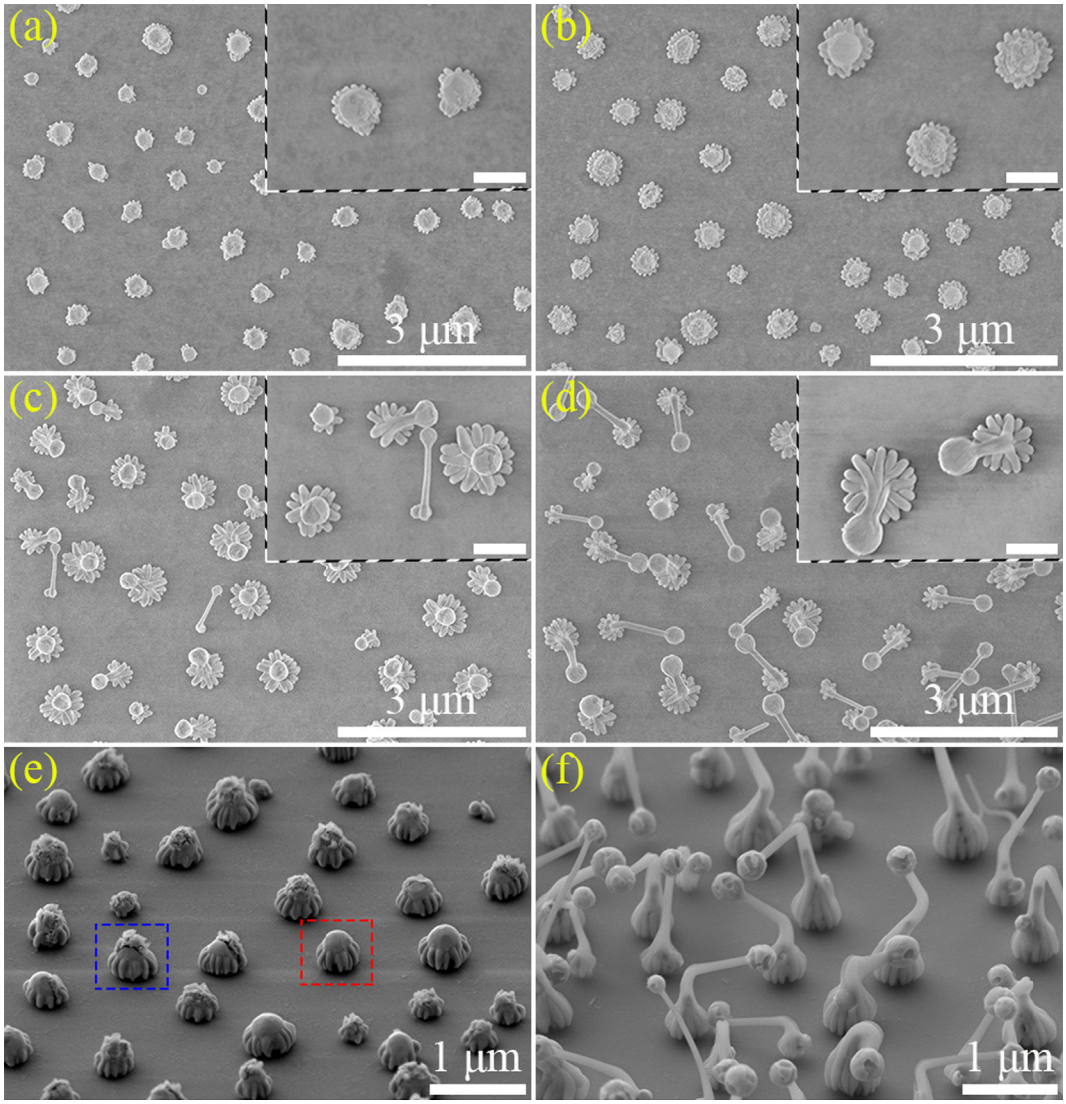

Fig. 2. SEM images of the nanostructures synthesized for different annealing times. The annealing times are 30 s, 60 s, 120 s, and 300 s from (a) to (d), respectively. Insets of (a-d) show higher magnifications (scale bar of insets: 500 nm). (e) and (f) are tilted views (at 54° tilt angle) for the 60 s and the 300 s samples, respectively.

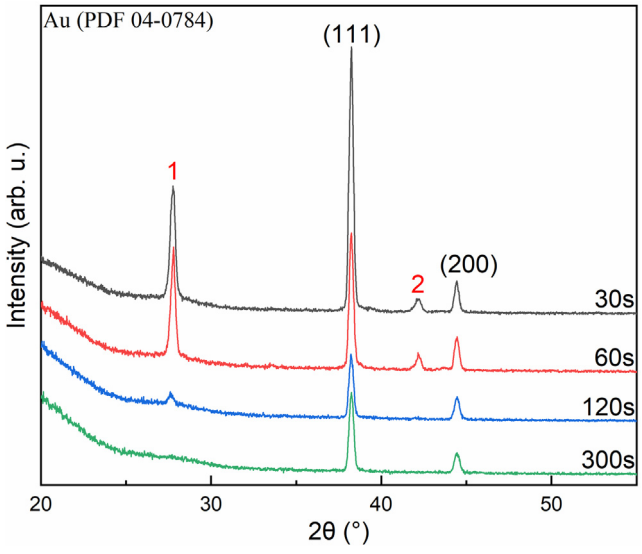

Fig. 3. Bragg-Brentano XRD diffractograms for samples heated for different annealing times. Au (111) and Au (200) reflexes are indexed according to PDF 04–0784 [30]. Reflexes 1 and 2 can be identified as Au silicide [32,33].

Table 1
Parameters from XRD results of Figs. 1 and 3 compared to powder diffraction data from the literature.

System	Intensity ratio of Au (111)/(200)	Peak position 1	Peak position 2
As-deposited sample	68.52 ± 0.20	–	–
30 s	7.77 ± 0.15	27.78° ± 0.08°	42.13° ± 0.10°
60 s	3.76 ± 0.30	27.80° ± 0.04°	42.16° ± 0.06°
120 s	2.60 ± 0.22	27.66° ± 0.06°	–
300 s	3.46 ± 0.12	–	–
Au (PDF 04–0784) [30]	1.9	–	–
Au_5Si_2 (PDF 36–0938) [32]	–	27.867° (203)	42.361° (107)
Au_2Si (PDF 40–1140) [33]	–	27.447° (631)	42.361° (773)

XRD results, the bright phase can be identified as Au and the dark phase as Au silicide in the smooth nanoflower, which also agrees with the EDS results of Fig. 4(b). Specifically, the upper Au makes the EDS results show a high Au concentration and the bottom Au silicide decreases the concentration of oxygen. On the other hand, in the rough nanoflower the bright part can be Au and the dark part should be SiO_x due to its higher oxygen concentration in the EDS spectra. Therefore, the difference in morphology of the surface of the nanoflowers stems from different phase compositions.

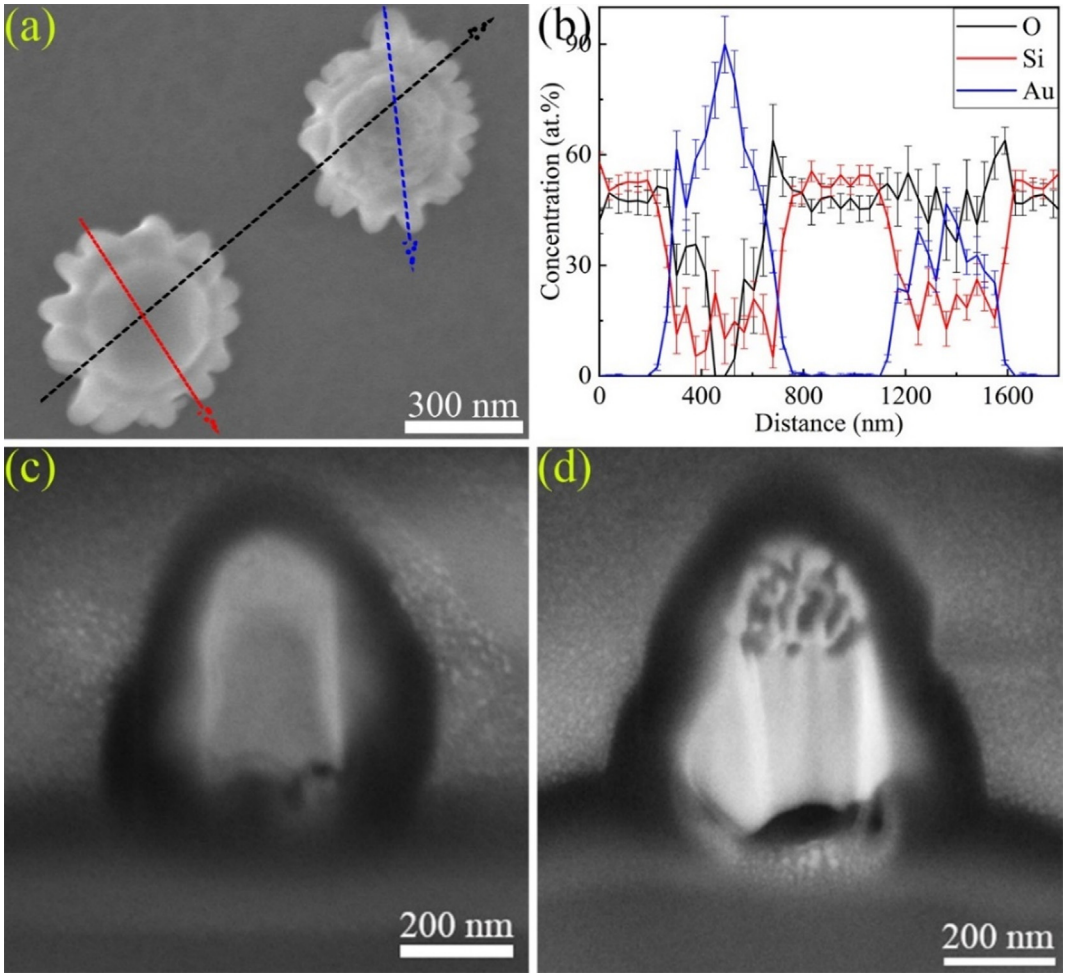

Fig. 4. EDS and FIB measurements for the 60 s sample. (a) Two nanoflowers show different surfaces, and three arrow lines with different colors indicate the EDS scanning paths. (b) EDS results along the black line in (a). Additional scans are included in Fig. S1 of the supporting information. (c) and (d) are the cross sections of nanoflowers with smooth and rough surfaces, respectively. The nanoflowers outlined with red and blue dash boxes in Fig. 2 are the morphologies of (c) and (d) before the FIB cutting, respectively.

The composition and phase distribution of the nanosprouts formed in the 300 s are analyzed in Fig. 5, where the element distributions of Fig. 5(b) show that the top nanoparticle contains Au, O, and Si with the latter presenting much higher concentration than the other two. The nanowire mainly contains Si and O, and the bottom part presents the same composition than the top nanoparticle but with different element concentrations. The EDS scan of the middle nanowire shows the existence of a small amount of Au along the longitudinal axis, and in addition a homogeneous distribution of Si and O across the radial direction. This indicates that the nanowire should consist of amorphous SiO_x. Fig. 5(c) shows the tilted views of two nanosprouts and their cross sections after FIB cutting in Fig. 5(d) exhibit a marked material contrast that suggests that different phases form in the top and in the bottom parts of the nanosprout. In the top nanoparticle, apart from the bright and dark contrasts, a thin grey layer can be observed around the dark area. Considering the alternate distributions of Si and Au in EDS results of Fig. S2, the dark region is identified as Si which is surrounded by a grey SiO_x layer, and the bright region in the top nanoparticle as Au, which also explains the high concentration of Si existing in the top nanoparticle of Fig. 5(b). Moreover, the brighter contrast of SiO_x than the black Si can be attributed to the existence of Au in SiO_x, as shows in Fig. S2, which indicates that the Au can also diffuse into the surrounding SiO_x layers. The cross section of the bottom part shows that it consists of a grey shell covering a bright nanoparticle with some dark parts inside which are also surrounded by a thin grey layer. Considering the EDS results, the bright nanoparticle is identified as Au which is covered by a shell of SiO_x nanobranches, and the dark parts inside the Au as Si which is surrounded by a grey SiO_x layer. These results indicate that the initial Au nanoparticle of the nanoflower splits in two forming the nanosprout, with the former covered by SiO_x nanobranches and the latter being elevated by a SiO_x nanowire.

Similar nanoflowers have been reported and the VLS mechanism was used to explain the obtained nanostructures. In those works, the Si source stemmed from active oxidation of Si within the holes etched by small Au nanoparticles at high temperature (volatile SiO) [15], or originated from the catalysis of Au nanoparticles on molten Si in the similar etch pits (Si vapor) [34]. In the present case, multiple circular regions appear in all samples, as shown in Fig. 6. At a glance, it is straightforward that these regions became larger with longer annealing times. The FIB cuts in Fig. 6(e-f) of one of these circular areas from the 60 s sample shows that the oxide layer within the circle disappeared and that the surface of the exposed Si substrate gradually sinks from the border to the center inside the circle, meaning that the circular area is a cavity. Fig. S3-S6 show that microstructures presenting two phases distribute inside the cavities.

To determine whether these cavities stem from the etching of the Au nanoparticles, a reference experiment is realized by anneal-

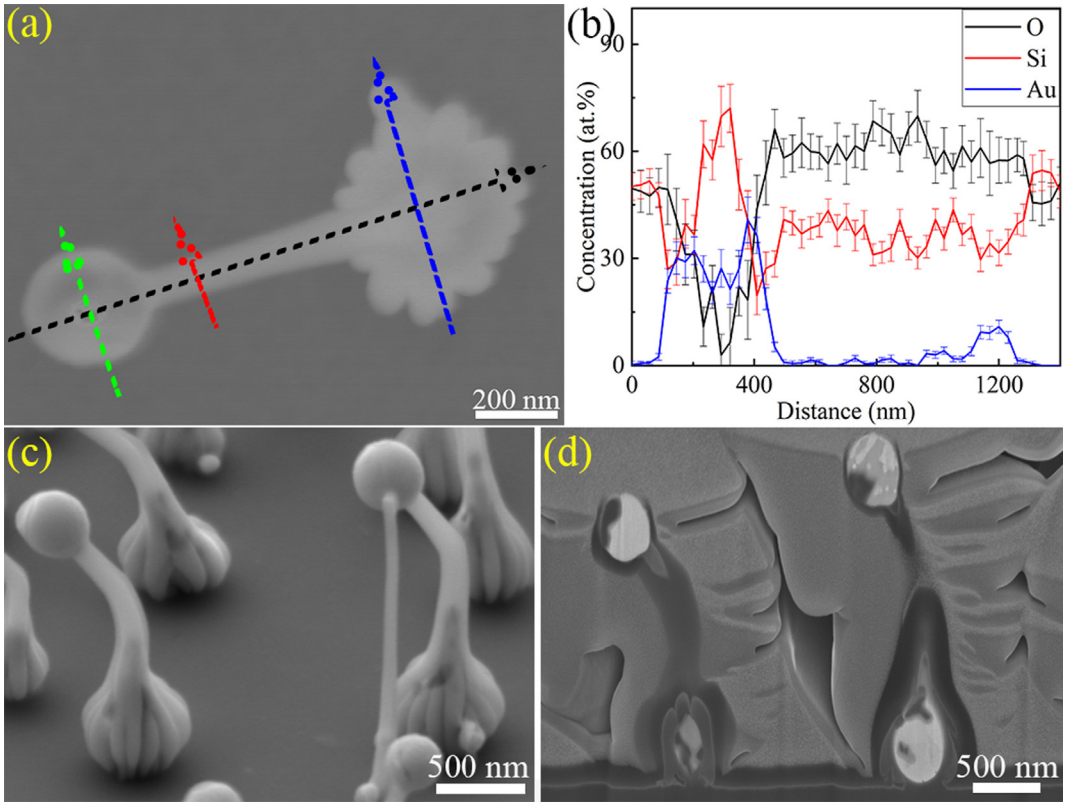

Fig. 5. EDS analysis and FIB cross-sectional images of the 300 s sample. (a) The arrow lines along different parts of a characteristic nanosprout show the EDS scanning paths. The EDS results along the black line are presented in (b) and the rest are included in Fig. S2 of the supporting information. Cross-sectional views of two nanosprouts before (c) and after (d) FIB cutting.

ing at 1050 °C for 60 s but replacing the forming gas of Ar + H_2 with Ar + O_2. As shown in Fig. 7(a-b), only faceted Au nanoparticles are formed by solid state dewetting [35–37], and there is no trace of the catalytic growth of other nanostructures since the surface of Au nanoparticles is quite clean. Also, the larger overview presented in Fig. S7(a) shows the absence of visible cavity-like structures piercing the SiO_2 barrier layer. Although Au nanoparticles are reported to penetrate the SiO_2 substrate in the presence of O_2 [38], this etching phenomenon is absent in the case of the Ar + O_2 experiment. Thus, the cavities in Fig. 6 are not the result of this kind of etching. Another reference experiment is conducted by keeping the same conditions than for sample 60 s but using a fused silica plate (SiO_2 substrate) to show the role of the Si substrate, and the results in Fig. 7(c-d) show that again only Au nanoparticles formed via solid state dewetting. An image showing a larger overview than those presented in Fig. 7 can be seen in Fig. S7(b) and it exhibits again the absence of cavities over the whole surface.

When H_2 or Si substrate are not present in the reference experiments, the Au thin film transforms to Au nanoparticles via solid state dewetting and the surfaces of the substrates do not present any special features. Contrary, the co-presence of H_2 or Si substrate leads to the formation of cavities and nanoflowers. This way, the formation of nanoflowers requires not only the dewetting of Au thin film, but also the catalytic growth SiO_x NWs. So, the formation of cavities should be directly related to the reaction with Si and a clear understanding of their formation of both cavity and SiO_x NWs is significant. Considering the circular morphology of these cavities together with the requirement for both H_2 and Si substrate, these characteristic cavities may originate from the SiO_2 decomposition which in turn, requires both Si as reactant and H_2 to create an O_2-deficient environment [19]. The cross sections in Fig. 6(e-f) also show some features that are in good agreement with the previous report [19], i.e., the unchanged Si/SiO_2 interface outside the cavity; the undercut near the oxide wall; the sunk Si surface inside the cavity; and the raised Si indicated by the arrow near the border of the cavity. Therefore, these circular cavities can be attributed to the reaction between the SiO_2 layer and Si substrate under high temperature and Ar + H_2 (reducing) environment. In addition, the enhancement of metallic thin films on the SiO_2 decomposition has been reported [25–27], Fig. S8 gives another group of reference experiment for samples without Au thin film on top. After RTP annealing in the reducing environment, no visible decomposed cavities can be observed when annealing times are 30 s and 60 s and very limited and small decomposed cavities can be found when annealing times are 120 s and 300 s, which clearly shows that the Au thin film can also enhance the SiO_2 decomposition in the present case.

The identification of the Si sources will help to understand the formation and evolution from nanoflowers to nanosprouts. Two potential sources might provide volatile SiO: decomposition of SiO_2 of the barrier layer and active oxidation of the exposed Si area. On the one hand, the volatile SiO from the decomposition of the 200 nm SiO_2 barrier layer may act as Si source. Although a previous work showed that the native oxide (about 3 nm) layer provides a negligible SiO amount to form NWs [28], the thickness of the oxide layer in the present case (200 nm) is considerably thicker. On the other hand, once the SiO_2 layer is removed, the exposed Si substrate can be actively oxidized forming volatile SiO which in turn can be another Si source. Because both processes are concurrent, is not possible to trigger only decomposition or active oxidation individually. Therefore, the amount of provided Si from each source is going to be estimated to identify which one dominates at each stage. Fig. 8 shows the height distribution of representative

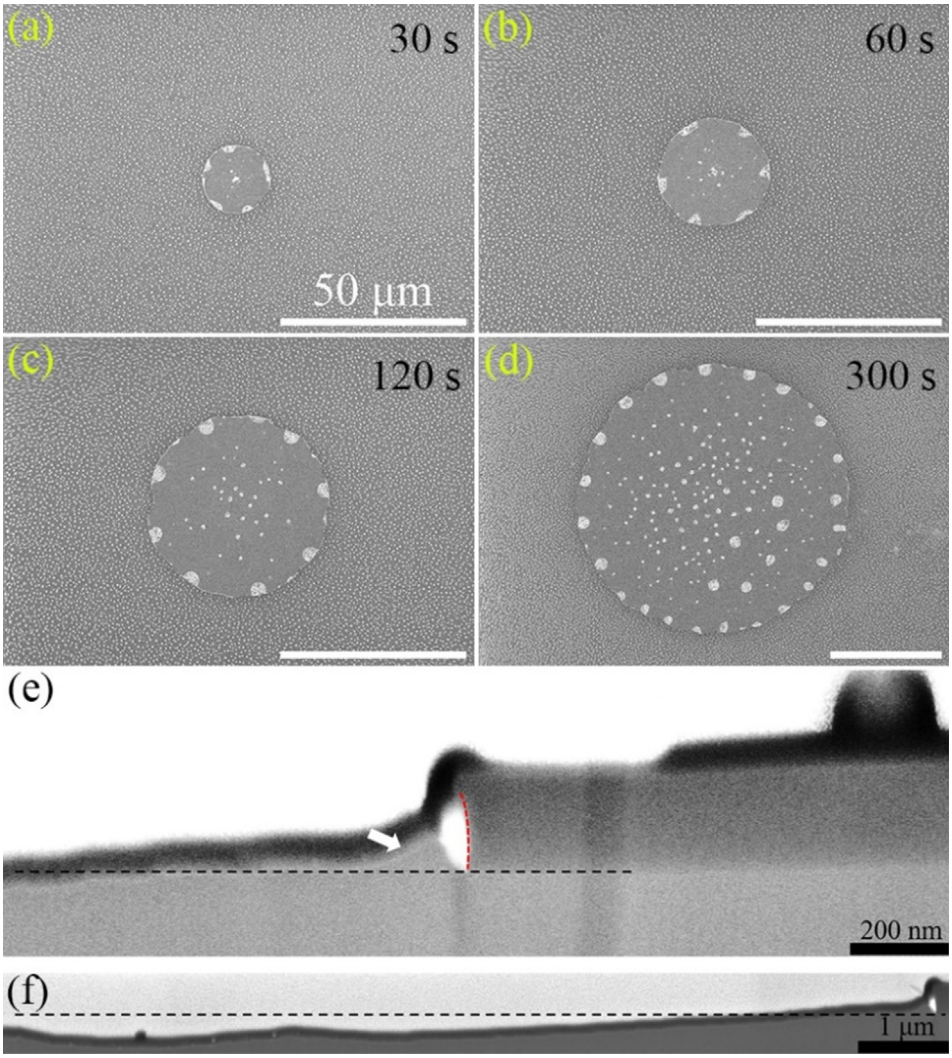

Fig. 6. SEM images of selected representative circular areas for different annealing times 30 s, 60 s, 120 s and 300 s from (a) to (d), respectively. Value of scale bar in (a) is also valid for (b) to (d). Cross section of a cavity in 60 s sample at border area (e) and wide view (f). The black dashed lines are the origin SiO_2/Si interface.

cavities of each system. Based on the cross-sectional images in Fig. 6(f), in Fig. 8(b) a schematic diagram of the cross section of a cavity is presented, in which the thickness of consumed SiO_2 and Si are marked as h_{SiO_2} and h_{Si}, respectively. The SiO_2 layer is totally consumed and then the h_{SiO_2} is 200 nm in this case because the Si exposes. The detailed calculations of h_{Si} are shown in the supporting materials in Fig. S9 and Table S1. As described above, the SiO_2 layer is decomposed employing the reaction $Si + SiO_2 \rightarrow 2SiO_{(g)}$; and when Si is exposed, the active oxidation reaction ($2Si + O_2 \rightarrow 2SiO_{(g)}$) may occur. Therefore, the ratio R of the amount of SiO from decomposition and from active oxidation can be obtained by the following equation:

$$R = \frac{2sh_{SiO_2}\rho_{SiO_2}}{m_{SiO_2}} : \left(\frac{sh_{Si}\rho_{Si}}{m_{Si}} - \frac{sh_{SiO_2}\rho_{SiO_2}}{m_{SiO_2}}\right) \quad (1)$$

Here, s is the area of the cavity. ρ_{SiO_2} (2.65 g/cm^3) and ρ_{Si} (2.33 g/cm^3) are the densities of SiO_2 and Si, and m_{SiO_2} (60 g/mol) and m_{Si} (28 g/mol) are the molar masses of SiO_2 and Si, respectively. Applying Eq. (1) to the different systems, the calculated ratios are shown in Table 2. This estimation shows that the SiO from SiO_2 decomposition is comparable to the SiO from active oxidation and therefore, it should contribute too to the growth of SiO_x nanostructures. Especially during the initial stage, the SiO from decomposition reaction may dominate as main Si source, and then the SiO from active oxidation prevails when the cavities became large enough for longer annealing times.

Three stages, void nucleation, coalescence, and total exposure of the Si substrate, have been reported during the decomposition of the SiO_2 layer [27]. For example, decomposed voids were believed to initiate at the pre-existing defects of the interface [23,24], and then they presented lateral expansion after these voids pierced to surface [26,39,40]. However, there are no experiments reporting how the volatile SiO escapes from the voids once it is formed at the interface and still covered by the oxide layer. The calculations confirm that the decomposition of the 200 nm thick SiO_2 layer is an important Si source for the growth of SiO_x NWs in the early stage. The overview of nanoflowers between two cavities in 60 s sample is shown in Fig. 9(a) to compare with the reported features that show that the morphologies of nanoflowers change with the distance to the hole and that the nanowires form inside the holes too [15,34]. The homogeneity represented by the similar nanoflowers of Fig. 9(b1-b4) and the homogeneous average particle sizes of Fig. S10 clearly indicate the formation mechanisms proposed in the previous papers cannot totally explain the phenomena in the present case.

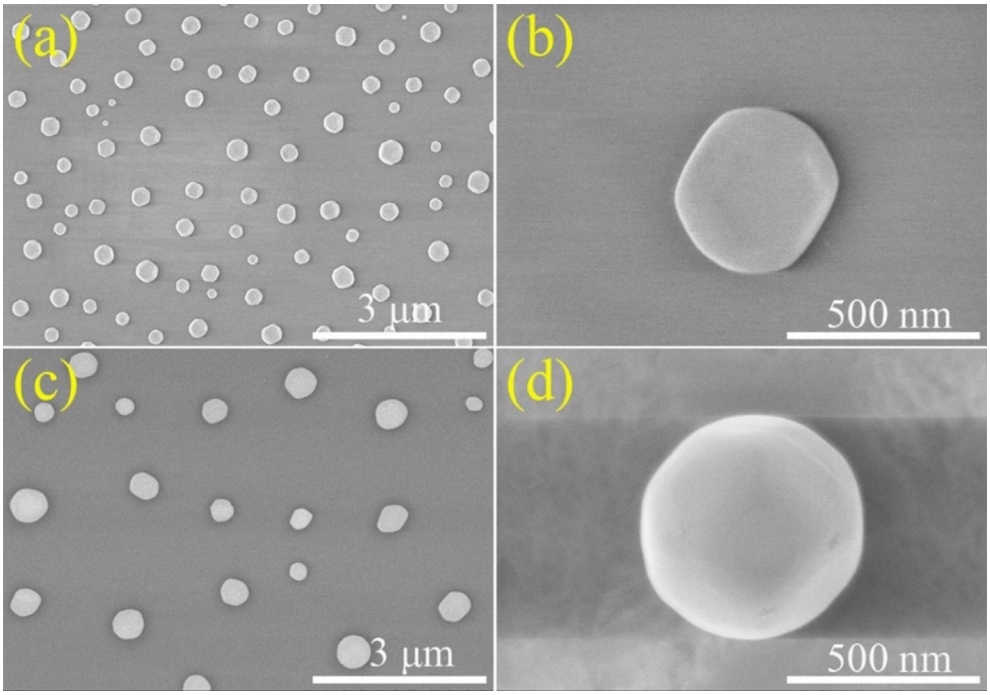

Fig. 7. (a, b) SEM images of Au nanoparticles formed on SiO_2(200 nm)/Si substrate under Ar + O_2 gas atmosphere, low (a) and high (b) magnifications, respectively. (c, d) Au nanoparticles formed on a SiO_2 substrate under Ar + H_2 gases, low (c) and high (d) magnifications, respectively. The annealing time was 60 s for both experiments.

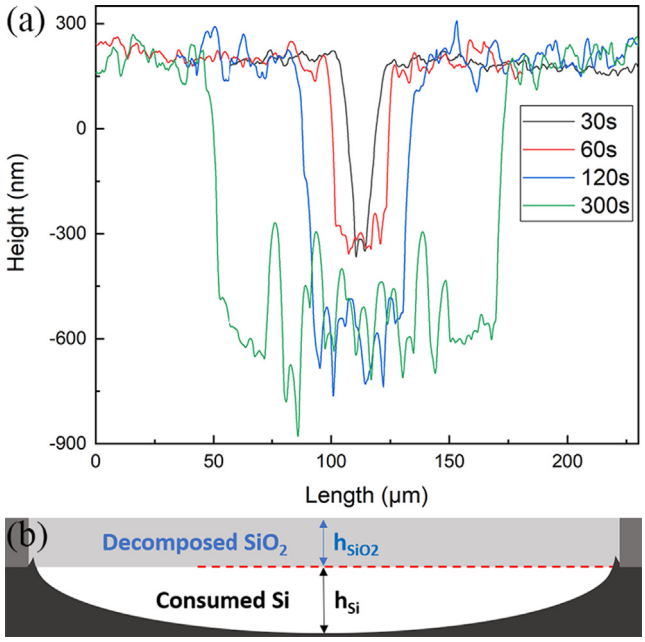

Fig. 8. (a) Height distributions of the characteristic selected cavities. Three cavities were measured for each sample and the complete results are shown in Fig. S9. (b) Schematic representation of the cross-sectional view of a cavity.

Table 2
Obtained ratios *R* of the amount of SiO from decomposition over from active oxidation for each sample.

30 s	60 s	120 s	300 s
1.00 ± 0.07	1.08 ± 0.02	0.46 ± 0.01	0.45 ± 0.02

In order to explain the homogeneous distribution of nanoflowers at the early stage and the transformation from nanoflowers to nanosprouts with longer annealing time, a mechanism is schematically proposed in Fig. 10. Several metallic atoms, like Ag, Au, and Cu, could diffuse to the SiO_2/Si interface to enhance the decomposition rate assisted by microchannels or microvoids in the oxide layer [25], and this enhancement of Au thin film has been proved in Fig. S8. Based on this, the proposed mechanism in Fig. 10 suggests that the SiO gas from the decomposition at the interphase SiO_2/Si may diffuse to the surface through these channels before the Si substrate is exposed by the forming cavities. The dash lines in Fig. 10(a) represent these microchannels. Once the volatile SiO gas meets with Au nanoparticles, the disproportionation of SiO happens ($2SiO \rightarrow Si + SiO_2$) [41]. The produced Si is absorbed by Au nanoparticles to form Au-Si droplets, while the SiO_2 is insoluble in the Au-Si droplets and can only move to the outer surface. The formation of new cavities dominates during the stage of void nucleation in the SiO_2 barrier layer [27]. Therefore, the main SiO source stems from the decomposition of SiO_2, and arrives to the Au nanoparticles from the bottom as noted in Fig. 10(a). As the above disproportionation reaction continues, several NWs nucleate at the bottom and grow along the surface of each Au-Si droplet because the mean size of the nanoparticles (Fig. S10) is large enough to provide several nucleation sites for NWs [15], leading to the formation of nanoflowers. The extra Si precipitates and then be oxidized to SiO_x NWs when the Au-Si droplets are supersaturated [41]. All the NWs are named with SiO_x NWs because they are formed in a O_2-deficient environment. The random distribution of microchannels in the oxide layer improves the homogeneity of the SiO gas, resulting in a more uniform morphology in Fig. 9.

This supply of SiO to the nanoparticles through the nanochannels might explain the different phases of the nanoflowers exhibited in Fig. 4. Because the Si source comes from below, the Au nanoparticles induced via solid state dewetting gradually transform to Au-Si droplets from the bottom to top. As a result of this,

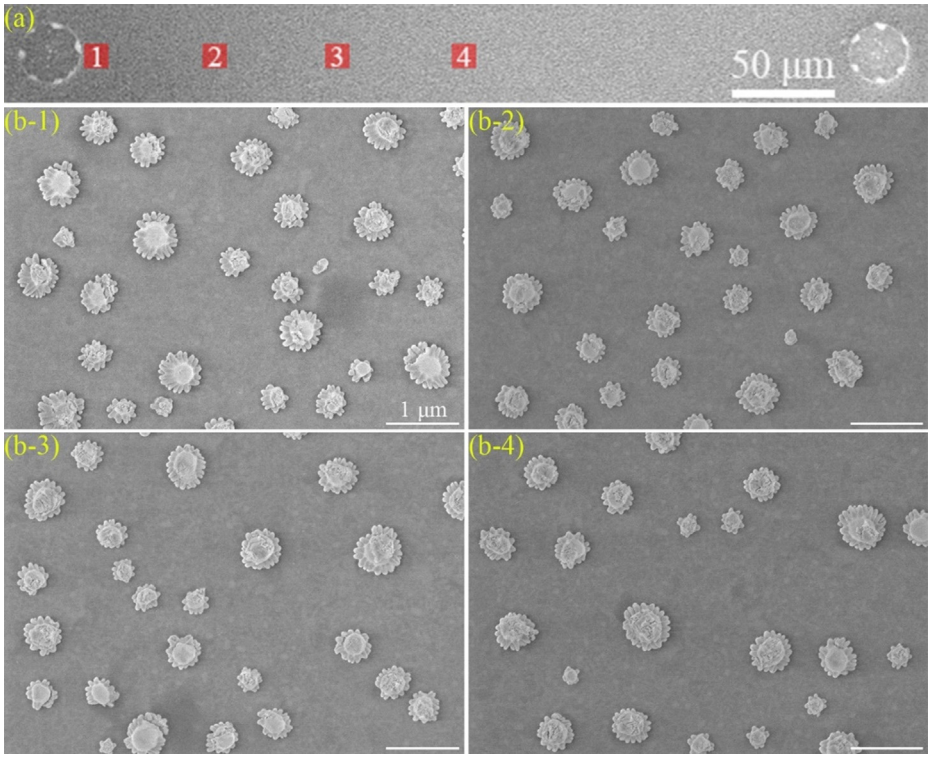

Fig. 9. Top view SEM images of the sample annealed for 60 s. (a) Region between two open cavities. (b1) - (b4) High magnification pictures taken in the areas 1–4 marked between in (a), respectively.

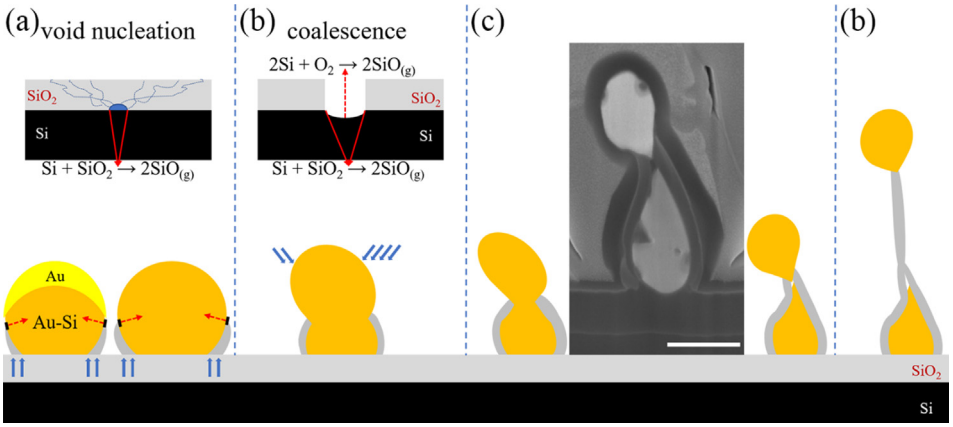

Fig. 10. Schematic diagrams of the evolution from nanoflower to nanosprout at high temperature. The upper diagrams in (a) and (b) are the states of decomposed cavities, corresponding to the early stage (void nucleation) and the second stage (coalescence) of decomposition. Different Si sources are noted by reaction equations and their directions are marked by blue arrows. The dash lines in (a) represent the nanochannels in the oxide layer. The schematic diagrams in (a) and (d) are representations of the tilted views of Fig. 1 and the cross sections of Figs. 4 and 5, respectively, while the evolution diagrams for the intermediate processes (b and c) are mainly based on the inset in Fig. 10(c). (scale bar for inset is 500 nm).

there should be different intermediate stages, as shown the schematic diagrams in Fig. 10(a) where the left one shows the partial transformation with the Au-Si droplet being covered by Au and surrounding SiO_x nanobranches and the right one shows that the Au nanoparticle fully transforms to Au-Si droplet. The heat treatment curves in Fig. 1(d) show that cooling rates slow down with the increasing annealing times. For nanoflowers, corresponding to 30 s and 60 s times, the temperature quickly drops below the Au-Si eutectic point. For partially transformed Au-Si droplets, the solid Au capping layer and surrounding SiO_x nanobranches may impose a compressive stress on the Au-Si droplets because of the volume expansion of droplets upon cooling. Together with fast cooling rate, it can retain the composition of Au-Si droplets till room temperature forming nanoflowers with smooth surfaces, which can also reasonably explain the occurrence of Au silicide reflex in the XRD spectrums of nanoflowers. By contrast, when the Au completely evolves to Au silicide droplets, the Au/Si phase separation will occur during the cooling stage even under high cooling rate conditions because there is no capping Au layer on the top of the droplets and then volume expansion cannot be well prevented. The fast cooling rates increase the number of Si nucleus and decrease their sizes, which favors the formation of many small Si pieces and these small Si can be fully oxidized by the residual oxygen in the chamber. Using this, the Au silicide covered by Au

can be obtained in Fig. 4(c), and the scattered SiO_x pieces on top of Au can be seen in Fig. 4(d).

When the coalescence stage of the decomposition starts, most of the cavities have exposed [27], and both the decomposition and the active oxidation coexist, as noted in Fig. 10(b). Then, the two Si sources emanate to the ambient and will incorporate into the droplets from their top, as indicated by the blue arrows in Fig. 10(b). Therefore, the main supply of Si changes from the bottom to the top of the droplets. At this point, the new nuclei would prefer to attaching the existing SiO_x nanobranches and grow along the perpendicular direction corresponding to the new liquid–solid interface [42], as indicated in Fig. 10(a), resulting in the gradual splitting of the Au-Si droplet (Fig. 10(b-c)). The inset in Fig. 10(c) shows a cross section for a nanosprout whose two nanoparticles are just divided. After the complete splitting of droplets, original growth directions of nanobranches will be hindered by each other and they will merge with other nanobranches into one thicker nanowire to reduce the surface energy. A similar phenomenon of merging has also been reported for several nanowires [43,44]. Hereafter, the merged SiO_x nanowire keeps growing and elevating the top nanoparticle, resulting in the formation of the sprout-like structure presented in Fig. 10 (d). The different phases in the nanosprouts can also be explained by the morphology conditions and the heat treatment curve in Fig. 1(d). Even if one of nanoparticles in the nanosprout is fully covered by SiO_x nanobranches, the much slower cooling rate makes the dwell time at temperatures above the eutectic point much longer, which may not only favor the phase separation of the droplets, but also assists the agglomeration of precipitated Si to form a big Si region in each part of the nanosprout, as shown in Fig. 5(d). Finally, only the Si near the border of the big region can be oxidized to SiO_x.

4. Conclusions

In the present work, Au-SiO_x flower-like and sprout-like heterostructures have been produced on a SiO_2/Si substrate during a rapid heat treatment. Two reference experiments confirm the need of both the reducing atmosphere and the Si substrate for the formation of the two heterostructures. It is explaining that the two different Si sources triggered during the annealing are responsible of the formation and evolution of these nanostructures. On the one hand, SiO gas from the decomposition of the SiO_2 layer can only penetrate the oxide layer through the nanochannels in the oxide layer when the Si substrate is still covered by the SiO_2 layer. On the other hand, the exposing of Si substrate due to the further SiO_2 decomposition introduces another SiO gas from the active oxidation of Si. The ratio between these sources shows that when nanoflowers are formed, both sources contribute similarly but in the case of the nanosprouts, it is the active oxidation who leads the process. In those cases, the direction of the Si source for the growth of SiO_x NWs changes from bottom to top of the central nanoparticles of nanoflowers, resulting in the splitting of the nanoparticles in two. As the further merging and growth of SiO_x NWs, one nanoparticle is covered by SiO_x NWs and the other is elevated, transforming the nanoflowers to nanosprouts.

The designing of Au/SiO_2/Si systems with a thick SiO_2 layer shows an easy-to-control way to alternate the main role between two Si sources. Furthermore, identifying the Si sources and unravelling their roles in the formation and evolution of these nanostructures allow us not only to tune the morphology of these nanoflowers and nanosprouts but also to introduce the change of the direction of the Si source as a tool for the tailored design of SiO_x nanostructures.

CRediT authorship contribution statement

Feitao Li: Data curation, Formal analysis, Investigation, Methodology, Visualization, Writing - original draft. **Manuel Oliva-Ramírez:** Conceptualization, Supervision, Investigation, Methodology, Writing - review & editing. **Dong Wang:** Conceptualization, Funding acquisition, Methodology, Supervision, Writing - review & editing. **Peter Schaaf:** Conceptualization, Methodology, Funding acquisition, Writing - review & editing.

Declaration of Competing Interest

The authors declare that they have no known competing financial interests or personal relationships that could have appeared to influence the work reported in this paper.

Acknowledgements

The work is supported by the Deutsche Forschungsgemeinschaft (DFG, grant Scha 632/20, ‘‘FunPartY”, grant Scha 632/24 within SPP ‘‘Tailored Disorder” and Scha 632/27 ‘‘DFG-Gerätezentrum”). This work is also supported by the free state of Thuringia under grants 2015 FGI 0025 305 (FastμXRD) and B715-10009 (BioMacroNano2020), all co-financed by the European Union within the framework of the European Regional Development Fund (ERDF). We are grateful to Mr. Joachim Döll from the TU Ilmenau, who helped in the preparation of the samples. We acknowledge support for the publication costs by the Open Access Publication Fund of the Technische Universität Ilmenau.

Data availability

The data that support the findings of this study are available from the corresponding author upon reasonable request.

Appendix A. Supplementary material

Supplementary data to this article can be found online at https://doi.org/10.1016/j.matdes.2021.109956.

References

[1] D. Dzhigaev, J. Svensson, A. Krishnaraja, Z. Zhu, Z. Ren, Y. Liu, S. Kalbfleisch, A. Björling, F. Lenrick, Z.I. Balogh, Strain mapping inside an individual processed vertical nanowire transistor using scanning X-ray nanodiffraction, Nanoscale 12 (27) (2020) 14487–14493.
[2] F.J. Wendisch, M. Abazari, H. Mahdavi, M. Rey, N. Vogel, M. Musso, O. Diwald, G.R. Bourret, Morphology-graded silicon nanowire arrays via chemical etching: Engineering optical properties at the nanoscale and macroscale, ACS appl. mater. Interfaces 12 (11) (2020) 13140–13147.
[3] A. Zhang, Y. Zhao, S.S. You, C.M. Lieber, Nanowire probes could drive high-resolution brain-machine interfaces, Nano Today 31 (2020) 100821.
[4] K. Yu, X. Pan, G. Zhang, X. Liao, X. Zhou, M. Yan, L. Xu, L. Mai, Nanowires in energy storage devices: structures, synthesis, and applications, Adv. Energy Mater. 8 (32) (2018) 1802369.
[5] Q. Li, N. Lu, L. Wang, C. Fan, Advances in nanowire transistor-based biosensors, Small Methods 2 (4) (2018) 1700263.
[6] C. Huang, A. Kim, D.J. Chung, E. Park, N.P. Young, K. Jurkschat, H. Kim, P.S. Grant, Multiscale engineered Si/SiO_x nanocomposite electrodes for lithium-ion batteries using layer-by-layer spray deposition, ACS appl. mater. Interfaces 10 (18) (2018) 15624–15633.
[7] C. Shen, R. Fu, H. Guo, Y. Wu, C. Fan, Y. Xia, Z. Liu, Scalable synthesis of Si nanowires interconnected SiO_x anode for high performance lithium-ion batteries, J. Alloys Compd. 783 (2019) 128–135.
[8] J. Zhang, X. Zhang, Z. Hou, L. Zhang, C. Li, Uniform SiO_x/graphene composite materials for lithium ion battery anodes, J. Alloys Compd. 809 (2019) 151798.
[9] J. Liu, T. Si, Z. Zhang, Mussel-inspired immobilization of silver nanoparticles toward sponge for rapid swabbing extraction and SERS detection of trace inorganic explosives, Talanta 204 (2019) 189–197.
[10] R.S. Wagner, W.C. Ellis, Vapor-Liquid-Solid mechanism of single crystal growth, Appl. Phys. Lett. 4 (5) (1964) 89–90.

[11] J.T.B.J. Kim, S. Kodambaka, M.C. Reuter, E.A. Stach, F.M. Ross, Kinetics of individual nucleation events observed in nanoscale Vapor-Liquid-Solid growth, Science 322 (5904) (2008) 1070–1073.
[12] R.Q. Zhang, Y. Lifshitz, S.T. Lee, Oxide-Assisted growth of semiconducting nanowires, Adv. Mater. 15 (78) (2003) 635–640.
[13] Y. Qin, X.N. Zhang, K. Zheng, H. Li, X.D. Han, Z. Zhang, Unusual catalyst-free epitaxial growth of silicon nanowires by thermal evaporation, Appl. Phys. Lett. 93 (6) (2008).
[14] P. Wu, X. Zou, L. Chi, Q. Li, T. Xiao, Growth model of lantern-like amorphous silicon oxide nanowires, Nanotechnology 18 (12) (2007).
[15] H. Luo, R. Wang, Y. Chen, D. Fox, R. O'Connell, J.J. Wang, H. Zhang, Enhanced photoluminescence from SiO_x–Au nanostructures, CrystEngComm 15 (46) (2013).
[16] W. Shi, H. Peng, Y. Zheng, N. Wang, N. Shang, Z. Pan, C. Lee, S. Lee, Synthesis of large areas of highly oriented, very long silicon nanowires, Adv. Mater. 12 (18) (2000) 1343–1345.
[17] Y. Zhang, Y. Tang, C. Lam, N. Wang, C. Lee, I. Bello, S. Lee, Bulk-quantity Si nanowires synthesized by SiO sublimation, J. Cryst. Growth 212 (1–2) (2000) 115–118.
[18] D. Wang, P. Schaaf, Silicon/silicide grown out of nanoporous gold nanoparticles, Phys. Status. Solidi A 210 (8) (2013) 1512–1515.
[19] R. Tromp, G.W. Rubloff, P. Balk, F.K. LeGoues, E.J. van Loenen, High-temperature SiO2 decomposition at the SiO_2/Si interface, Phys. Rev. Lett. 55 (21) (1985) 2332–2335.
[20] N. Miyata, M. Shigeno, Y. Arimoto, T. Ito, Thermal decomposition of native oxide on Si(100), J. Appl. Phys. 74 (8) (1993) 5275–5276.
[21] H. Hibino, M. Uematsu, Y. Watanabe, Void growth during thermal decomposition of silicon oxide layers studied by low-energy electron microscopy, J. Appl. Phys. 100 (11) (2006).
[22] Y. Enta, T. Nagai, T. Yoshida, N. Ujiie, H. Nakazawa, Decomposition kinetics of silicon oxide layers on silicon substrates during annealing in vacuum, J. Appl. Phys. 114 (11) (2013).
[23] K. Hofmann, G.W. Rubloff, R.A. McCorkle, Defect formation in thermal SiO_2 by high-temperature annealing, Appl. Phys. Lett. 49 (22) (1986) 1525–1527.
[24] K. Hofmann, G. Rubloff, M. Liehr, D. Young, High temperature reaction and defect chemistry at the Si/SiO_2 interface, Appl. Surf. Sci. 30 (1–4) (1987) 25–31.
[25] H. Dallaporta, M. Liehr, J.E. Lewis, Silicon dioxide defects induced by metal impurities, Phys. Rev. B 41 (8) (1990) 5075–5083.
[26] P. Bábor, R. Duda, J. Polčák, S. Průša, M. Potoček, P. Varga, J. Čechal, T. Šikola, Real-time observation of self-limiting SiO_2/Si decomposition catalysed by gold silicide droplets, RSC Adv. 5 (123) (2015) 101726–101731.
[27] F. Leroy, T. Passanante, F. Cheynis, S. Curiotto, E.B. Bussmann, P. Müller, Catalytically enhanced thermal decomposition of chemically grown silicon oxide layers on Si(001), Appl. Phys. Lett. 108 (11) (2016).
[28] T.H. Kim, A. Shalav, R.G. Elliman, Active-oxidation of Si as the source of vapor-phase reactants in the growth of SiO_x nanowires on Si, J. Appl. Phys. 108 (7) (2010).
[29] H. Hijazi, F. Leroy, G. Monier, G. Grégoire, E. Gil, A. Trassoudaine, V.G. Dubrovskii, D. Castelluci, N.I. Goktas, R.R. LaPierre, Y. André, C. Robert-Goumet, Dynamics of Gold Droplet Formation on SiO_2/Si(111) Surface, J. Phys. Chem. C 124 (22) (2020) 11946–11951.
[30] H.E. Swanson, Standard X-ray diffraction powder patterns, US Department of Commerce, National Bureau of Standards 1 (1953) 23–33.
[31] M. Oliva-Ramirez, P. Schade, C. Zobel, D. Wang, P. Schaaf, Morphological and compositional mapping of supersaturated AuNi alloy nanoparticles fabricated by solid state dewetting, Appl. Surf. Sci. Advances 4 (2021) 100082.
[32] B. Tsaur, J. Mayer, Metastable Au-Si alloy formation induced by ion-beam interface mixing, Philos. Mag. A 43 (2) (1981) 345–361.
[33] L. Hultman, A. Robertsson, H. Hentzell, I. Engström, P. Psaras, Crystallization of amorphous silicon during thin-film gold reaction, J. Appl. Phys. 62 (9) (1987) 3647–3655.
[34] P. Zhang, Y. Cui, SiO_x nanostructures grown under atmospheric pressure, CrystEngComm 15 (46) (2013) 9963–9967.
[35] D. Wang, P. Schaaf, Two-dimensional nanoparticle arrays formed by dewetting of thin gold films deposited on pre-patterned substrates, J. Mater. Sci. Mater. Electron. 22 (8) (2010) 1067–1070.
[36] D. Wang, R. Ji, P. Schaaf, Formation of precise 2D Au particle arrays via thermally induced dewetting on pre-patterned substrates, Beilstein J. Nanotechnol. 2 (2011) 318–326.
[37] M. Oliva-Ramirez, D. Wang, D. Flock, V. Rico, A.R. Gonzalez-Elipe, P. Schaaf, Solid-state dewetting of gold on stochastically periodic SiO_2 nanocolumns prepared by oblique angle deposition, ACS Appl. Mater. Interfaces 13 (9) (2021) 11385–11395.
[38] L.J. de Vreede, A. van den Berg, J.C. Eijkel, Nanopore fabrication by heating Au particles on ceramic substrates, Nano Lett. 15 (1) (2015) 727–731.
[39] K.E. Johnson, T. Engel, Direct measurement of reaction kinetics for the decomposition of ultrathin oxide on Si(001) using scanning tunneling microscopy, Phys. Rev. Lett. 69 (2) (1992) 339–342.
[40] H.W. Noriyuki Miyata, Masakazu Ichikawa, Thermal Decomposition of an Ultrathin Si Oxide Layer around a Si(001)- (2×1) Window, Phys. Rev. Lett. 84 (5) (2000) 1043–1046.
[41] W. Dewald, C. Borschel, D. Stichtenoth, T. Niermann, C. Ronning, Phase diagram of Si nanowire growth by disproportionation of SiO, J. Cryst. Growth 312 (10) (2010) 1751–1754.
[42] F. Panciera, Y.C. Chou, M.C. Reuter, D. Zakharov, E.A. Stach, S. Hofmann, F.M. Ross, Synthesis of nanostructures in nanowires using sequential catalyst reactions, Nat. Mater. 14 (8) (2015) 820–825.
[43] S. Fan, S. Zhao, X. Liu, Z. Mi, Study on the coalescence of dislocation-free GaN nanowires on Si and SiO_x, J. Vac. Sci. Technol. B 32 (2) (2014) 02C114.
[44] L. Cheng, J. Su, X. Zhu, Athermal coalescence of two parallel and contacting amorphous SiO_x nanowires as induced by uniform e-beam irradiation, Mater. Lett. 237 (2019) 286–289.